Magnetic anisotropy of polycrystalline high-temperature ferromagnetic MnxSi1-x (x≈0.5) alloy films

Drovosekova, A. B.; Kreines, N. M.; Savitsky, A. O.; Kapelnitsky, S. V.; Rylkov, V. V.; Tugushev, V. V.; Prutskov, G. V.; Novodvorskii, O. A.; Shorokhova, A. V.; Wang, Y.; Zhou, S.;

Originally published:

January 2017

Journal of Magnetism and Magnetic Materials 429(2017), 305-313

DOI: https://doi.org/10.1016/j.jmmm.2017.01.022

Magnetic anisotropy of polycrystalline high-temperature ferromagnetic Mn_xSi_{1-x} ($x \approx 0.5$) alloy films

A.B. Drovosekov[a,*], N.M. Kreines[a], A.O. Savitsky[a], S.V. Kapelnitsky[b,c], V.V. Rylkov[b,d], V.V. Tugushev[b,e], G.V. Prutskov[b], O.A. Novodvorskii[f], A.V. Shorokhova[f], Y. Wang[g], S. Zhou[g]

[a] *P.L.Kapitza Institute for Physical Problems RAS, Kosygina St. 2, 119334 Moscow, Russia*
[b] *National Research Centre "Kurchatov Institute", Kurchatov Sq. 1, 123182 Moscow, Russia*
[c] *Institute of Physics and Technology RAS, Nakhimovsky av. 36, build 1, 117218 Moscow, Russia*
[d] *Kotel'nikov Institute of Radio Engineering and Electronics RAS, 141190 Fryazino, Moscow region, Russia*
[e] *Prokhorov General Physics Institute RAS, Vavilov St. 38, 119991 Moscow, Russia*
[f] *Institute on Laser and Information Technologies RAS, Svyatoozerskaya St. 1, 140700 Shatura, Moscow region, Russia*
[g] *Helmholtz-Zentrum Dresden-Rossendorf, Institute of Ion Beam Physics and Materials Research, Bautzner Landstrasse 400, 01328 Dresden, Germany*

Abstract

A set of thin film Mn_xSi_{1-x} alloy samples with different manganese concentration $x \approx 0.44 - 0.63$ grown by the pulsed laser deposition (PLD) method onto the Al_2O_3 (0001) substrate was investigated in the temperature range 4 – 300 K using ferromagnetic resonance (FMR) measurements in the wide range of frequencies ($f = 7 - 60$ GHz) and magnetic fields ($H = 0 - 30$ kOe). For samples with $x \approx 0.52 - 0.55$, FMR data show clear evidence of ferromagnetism with high Curie temperatures $T_C \sim 300$ K. These samples demonstrate complex and unusual character of magnetic anisotropy described in the frame of phenomenological model as a combination of the essential second order easy plane anisotropy contribution and the additional forth order uniaxial anisotropy contribution with easy direction normal to the film plane. We explain the obtained results by a polycrystalline (mosaic) structure of the films caused by the film-substrate lattice mismatch. The existence of extra strains at the crystallite boundaries leads to an essential inhomogeneous magnetic anisotropy in the film plane.

Keywords: magnetic Mn_xSi_{1-x} alloy films, magnetic anisotropy, ferromagnetic resonance
PACS: 75.70.-i, 75.30.Gw, 76.50.+g

1. Introduction

Development of Si based magnetic semiconductor materials for spintronic applications attracts a lot of attention, since these materials can be easily incorporated into the existing microelectronic technology [1]. In particular, Si-Mn alloys demonstrating unusual magnetic and transport properties [2–8] have especial interest to engineer non-conventional integrated-circuit elements.

However, there exist significant technological and fundamental obstacles to adapt Si-Mn based elements to the needs of spintronic. At relatively low Mn content in Mn_xSi_{1-x} alloys ($x = 0.05 - 0.1$), the ferromagnetism (FM) at above room temperature has been revealed. But these alloys turn out to be strongly inhomogeneous materials due to their phase segregation, leading to formation of isolated magnetic $MnSi_{1.7}$ precipitate nanoparticles with the Mn content $x \approx 0.35$ in Si matrix [2]. In such alloys, anomalous Hall effect testifying the spin polarization of carriers is absent, that makes impossible to use these materials in spintronic applications. At the same time, the fabrication of well-reproducible homogeneous magnetic alloys with high Mn content $x \approx 0.35$ is difficult because of the variety of stable phases of high $MnSi_y$ silicides (not less than five) with the close content of components ($y = 1.72 - 1.75$) [6, 7].

In contrast, nonstoichiometric Mn_xSi_{1-x} alloys with high Mn content ($x \approx 0.5$, i.e. close to stoichiometric MnSi) are not inclined to a phase segregation and formation of isolated magnetic precipitates, so they seem more promising for spintronic applications than dilute Mn_xSi_{1-x} alloys. Recently we have found that in thin films of such concentrated alloys, the Curie temperature T_C increases by more than an order of magnitude as compared with bulk MnSi ($T_C \approx 30$ K) [6]. Comparative studies of anomalous Hall effect and transverse Kerr effect showed that the ferromagnetic transition in Mn_xSi_{1-x} ($x \approx 0.52 - 0.55$) alloys occurring at $T \sim 300$ K, has a global nature and is not associated with the phase segregation [7]. Besides high T_C values, the films investigated in [6, 7] show large values of saturation magnetization reaching ≈ 400 emu/cm^3 at low temperatures. The observed magnetization value corresponds to $\approx 1.1\ \mu_B$/Mn, that significantly exceeds the value 0.4 μ_B/Mn typical for bulk MnSi crystal [9].

High temperature FM in Mn_xSi_{1-x} ($x \approx 0.5$) alloys has been qualitatively interpreted [6, 7] in frame of the early proposed model for dilute Mn_xSi_{1-x} alloys [3], i.e. in terms of complex defects with local magnetic moments embedded into the matrix of itinerant FM. However, many details of FM order in Mn_xSi_{1-x} ($x \approx 0.5$) alloys are still not completely clear due to

*Corresponding author
Email address: drovosekov@kapitza.ras.ru (A.B. Drovosekov)

insufficient experimental studies. In particular, there are no data on their magnetic anisotropy features. In the present work, thin Mn_xSi_{1-x} ($x \approx 0.52 - 0.55$) films are investigated by the ferromagnetic resonance (FMR) method which is powerful for providing valuable information about magnetic anisotropy peculiarities of thin film magnetic materials, in particular, like dilute magnetic semiconductors (see [10] and references therein). Our studies are largely focused on the position and shape of FMR signal, while the analysis of the refinements of the line width data providing additional information on the magnetic inhomogeneity and relaxation rate of magnetization is not presented in this work. Besides, to study the details of crystalline and magnetic microstructures of our films we perform in this work the atomic force microscopy (AFM) and magnetic force microscopy (MFM) investigations. We hope that AFM and MFM methods allow for additional understanding of the FMR results, since these methods are able to reveal the "local" effects of the crystal and magnetic texture of the film on the origin of magnetic anisotropy established in FMR measurements.

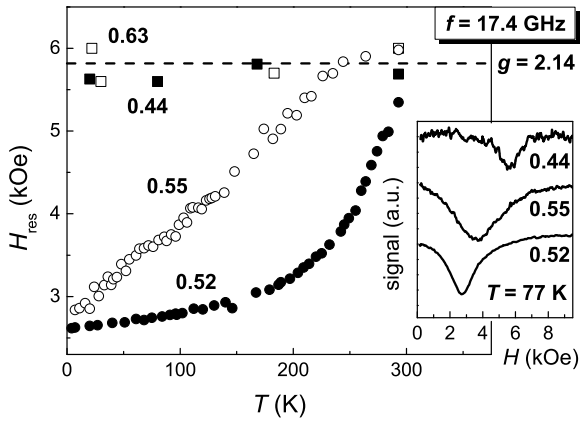

Figure 1: Temperature dependence of the resonance field $H_{res}(T)$ at the frequency 17.4 GHz for samples with different manganese concentration. The dashed line corresponds to the calculated position of paramagnetic resonance for g-factor $g = 2.14$. The inset demonstrates examples of the experimental resonance spectra at $T = 77$ K. The field is applied in the film plane.

2. Samples and experimental details

We studied six samples with manganese content in the range $x \approx 0.44 - 0.63$. The 70 nm thick film samples were produced by the pulse laser deposition (PLD) method on Al_2O_3 (0001) substrates at 340 °C. The composition of the films was testified by X-ray photoelectronic spectroscopy (for details see [6]).

The structural properties of the samples were studied by X-ray diffraction (XRD) analysis using a Rigaku SmartLab diffractometer without monochromators and a diaphragm before the detector. In this case, intensity of the direct beam was as high as $1.5 \cdot 10^9$ pulses/s. Additionally, we performed room temperature AFM and MFM investigations in the sample Mn_xSi_{1-x} ($x \approx 0.52$) having the most pronounced high-T_C FM, using microscope SmartSPM (AIST-NT).

FMR spectra of the obtained samples were studied at temperatures $T = 4 - 300$ K in the wide range of frequencies ($f = 7 - 60$ GHz) and magnetic fields ($H = 0 - 30$ kOe). To detect the resonance absorption signal, magnetic field dependencies of the microwave power transmitted through the cavity resonator with the sample inside were measured at constant frequency. Measurements were carried out for different orientations of the magnetic field with respect to the film plane.

3. Experimental results and discussion

3.1. FMR measurements

The dependence of the resonance field on temperature in case of the field applied in the film plane is shown in Fig.1 for several samples. Films with Mn concentration $x \approx 0.44$ and $x \approx 0.63$ demonstrate the resonance absorption peak in the field corresponding to a paramagnetic resonance situation, i.e. $f = \gamma H$, with the gyromagnetic ratio $\gamma \approx 3$ GHz/kOe corresponding to the g-factor value $g = 2.14$, which is in agreement with the value reported in Ref. [11] for the bulk MnSi single crystal. The paramagnetism of the samples with $x \approx 0.44$ and $x \approx 0.63$ is observed in the temperature range 20 – 300 K, that is in accordance with the results of Ref. [6].

At low temperatures in the range of concentrations $x \approx 0.52 - 0.55$, the films show significant shift of absorption peak into the region of smaller fields with respect to paramagnetic samples (Fig.1). As the temperature increases, the resonance field also increases and at $T \sim 300$ K reaches the value corresponding to the paramagnetic resonance situation. The observed absorption lines have the Lorentz-like shape, and the resonance field anisotropy in the film plane is absent.

The shift of the FMR absorption line revealed in our measurements (shown in Fig.1) clearly indicates the presence of FM moment in samples with $x \approx 0.52 - 0.55$ at low temperatures, in agreement with Ref. [6]. When the external magnetic field H is applied in the plane of a thin FM film with magnetization M, the FMR frequency $f_{\|}$ may be described by the phenomenological formula (see Appendix A):

$$f_{\|} = \gamma \sqrt{H(H + K_{\|}M)}. \quad (1)$$

Here $K_{\|}$ is the effective easy plane magnetic anisotropy coefficient; $K_{\|}M$ is the effective field of easy plane magnetic anisotropy. This field describes the effect of two factors on the FMR spectra: 1) the shape magnetic anisotropy depending of the form of the sample and 2) the crystal structure driven magnetic anisotropy which is due to relativistic interactions between electrons and ions in the sample material. Following a simplest model used in Ref. [12] it is easy to obtain:

$$K_{\|}M = 4\pi M + \frac{2K_1}{M}, \quad (2)$$

where K_1 is the phenomenological constant of the second-order easy plane crystal structure driven magnetic anisotropy. In the absence of K_1, Eq.(1) transforms into the well known Kittel formula for the applied field H lying in the film plane [13].

According to Eq.(1), a reduction of FM moment of the film with increasing temperature leads to a decrease of the FMR line

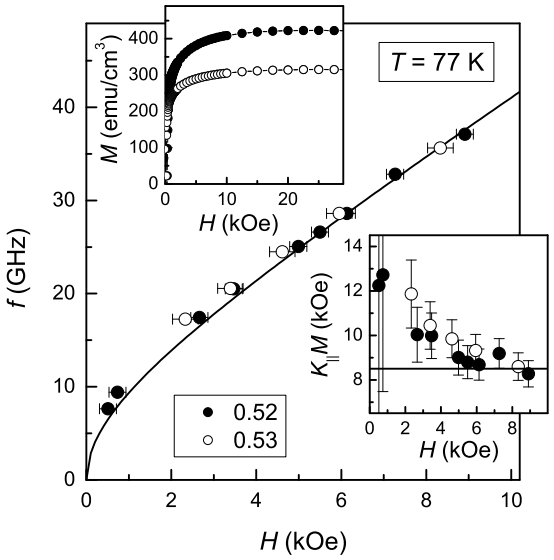

Figure 2: Dependence of the resonance frequency on the magnetic field applied in the film plane for samples with $x \approx 0.52$ and $x \approx 0.53$ at $T = 77$ K. Points are experimental data; the line is the theoretical curve according to Eq.(1). The insets represent static magnetization curves (the upper inset) and the value of the parameter $K_{\|}M$ in Eq.(1) as a function of magnetic field (the bottom inset).

shift with respect to the paramagnetic resonance situation. Thus FMR data (Fig.1) confirm the FM order up to $T \sim 300$ K in samples with Mn concentration $x \approx 0.52 - 0.55$.

Dependencies of the FMR frequency on the magnetic field applied in the film plane for samples with Mn concentrations 0.52 and 0.53 at $T = 77$ K are shown in Fig.2. At sufficiently high fields $H > 5$ kOe (i.e. in the high-frequency region $f > 25$ GHz), the $f(H)$ dependence can be well approximated by Eq.(1) with the field-independent value $K_{\|}M \approx 8.7$ kOe (at $T = 77$ K both samples have about the same $K_{\|}M$ values). However, some deviations of the experimental points from the theoretical curve are observed at smaller fields. In the bottom inset of Fig.2, the experimentally obtained field dependence of $K_{\|}M$ parameter is shown. One can see that the value of $K_{\|}M$ parameter significantly depends on the applied field at small fields $H < 5$ kOe, while it comes nigh unto a saturation at higher fields $H > 5$ kOe.

The observed deviation of the $K_{\|}M$ parameter at low fields from the constant value at high fields is probably due to a random distribution of local magnetic anisotropy axes in the sample plane resulting in inhomogeneity of magnetization at low applied fields. Indeed, static magnetization curves (upper inset in Fig.2) achieve a saturation in relatively high fields $H \sim 5$ kOe. One can notice, however, that the $K_{\|}M$ parameter estimated from the FMR data increases as the magnetic field decreases below 5 kOe, while the static magnetization diminishes. This contradiction clearly shows inapplicability of Eq.(1) in the region of small fields and indicates inhomogeneity of local magnetization and anisotropy. Below in this work, only FMR data obtained at high frequencies $f > 25$ GHz are taken into account to estimate the magnetic anisotropy parameters of the system. Such frequencies provide sufficiently high resonance fields $H > 5$ kOe, where the FMR data can be well approximated in frame of Kittel's formalism (Eq.(1)).

Temperature dependencies of the $K_{\|}M$ parameter obtained by means of Eq.(1) for the films with Mn concentration $x \approx 0.52 - 0.55$ are given in Fig.3. For all the samples, the low temperature value of the $K_{\|}M$ parameter is about 10 kOe (see Table 1). The $K_{\|}M(T)$ curve for the sample with $x \approx 0.52$ has the Brillouin-like shape with $T_C \approx 300$ K. Note that the Brillouin curve gives smaller T_C value than found from static magnetization measurements [6] (more precisely $M(T)$ dependence can be fitted within spin-fluctuation model [3]; see Fig.3 and [6]). For the films with $x \geq 0.53$, the curve $K_{\|}M(T)$ is closer to the linear dependence: this fact can be caused by a heterogeneity of samples that is also confirmed by a larger line width of the samples with $x \approx 0.53 - 0.55$ in comparison with the case $x \approx 0.52$ (see the inset in Fig.1).

Besides the experimental $K_{\|}M(T)$ curves, Fig.3 represents the temperature dependencies of the demagnetizing field $4\pi M$ calculated from static magnetization data at $H = 10$ kOe applied in the film plane. The shapes of the $K_{\|}M(T)$ and $4\pi M(T)$ curves are close to each other, while the low temperature values of $K_{\|}M$ parameter exceed $4\pi M$ considerably (about two times; see Table 1). These two values equalize only in the vicinity of T_C. In frame of the phenomenological model exposed in Appendix A, the large difference between $K_{\|}M$ and $4\pi M$ can be explained by the fact that the crystal structure driven second order easy plane magnetic anisotropy is comparable with the sample shape magnetic anisotropy. The similarity of the $M(T)$ and $K_{\|}M(T)$ curves means that $K_{\|}$ is almost temperature independent and consequently $K_1(T) \sim M(T)^2$. The inset in Fig.3 demonstrates the resulting temperature dependence of the K_1 constant.

To obtain further insight into the peculiarities of the magnetic anisotropy of our system, the $f(H)$ dependencies were investigated for samples with $x \approx 0.52$ and $x \approx 0.53$ at $T = 4.2$ K, when the applied field was perpendicular to the film plane (Fig.4).

Within the phenomenological model exposed in Appendix A, in this case the FMR frequency $f_{\perp}$ in the saturation regime has a linear dependence on the applied external field:

$$f_{\perp} = \gamma(H - K_{\perp}M), \qquad (3)$$

where $K_{\perp}$ is the effective hard axis magnetic anisotropy coef-

Table 1: Effective demagnetization, anisotropy fields and corresponding anisotropy constants deduced for samples with Mn content $x \approx 0.52$, 0.53 and 0.54 at $T = 4.2$ K using Eqs.(1–4).

x	$4\pi M$	$K_{\|}M$	$K_{\perp}M$	K_1	K_2
	(kOe)			(10^6 erg/cm^3)	
0.52	5.5	9.0	6.4	0.8	−0.3
0.53	4.1	10.8	8.7	1.1	−0.2
0.54	3.9	9.5	no data	0.9	no data

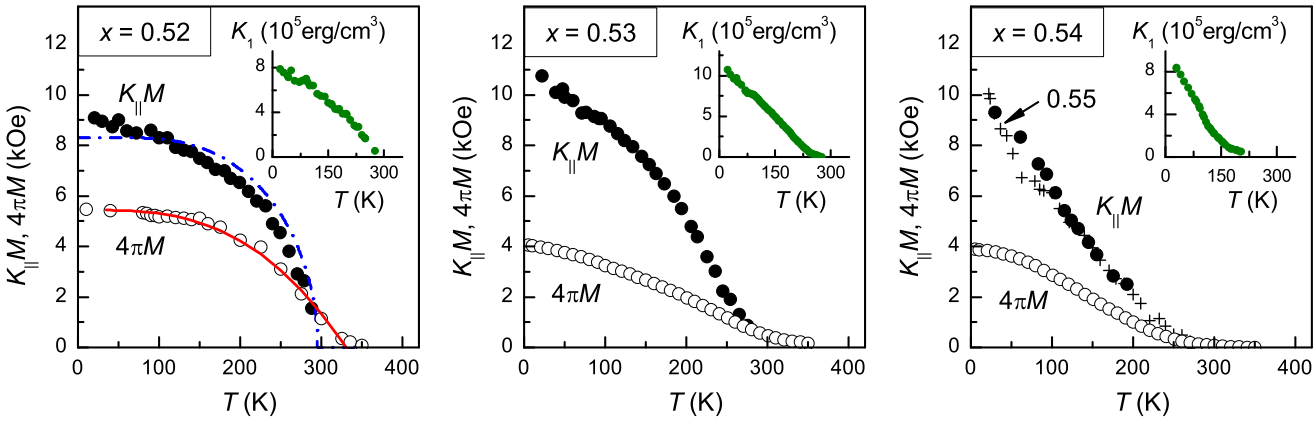

Figure 3: Temperature dependence of $K_{\|}M$ parameter (solid circles) obtained from FMR, and demagnetizing field $4\pi M$ (open circles) obtained from static magnetization data for samples with concentration $x \approx 0.52, 0.53$ and 0.54. The dash dot line (blue) in the left plot represents Brillouin curve $K_{\|}M(T)$ for spin 1/2; the solid line (red) is theoretical $4\pi M(T)$ curve determined in [6] within the framework of the spin-fluctuation model [3]. Crosses in the right plot represent $K_{\|}M(T)$ dependence for $x \approx 0.55$. The insets show experimental temperature dependencies of the anisotropy constant K_1.

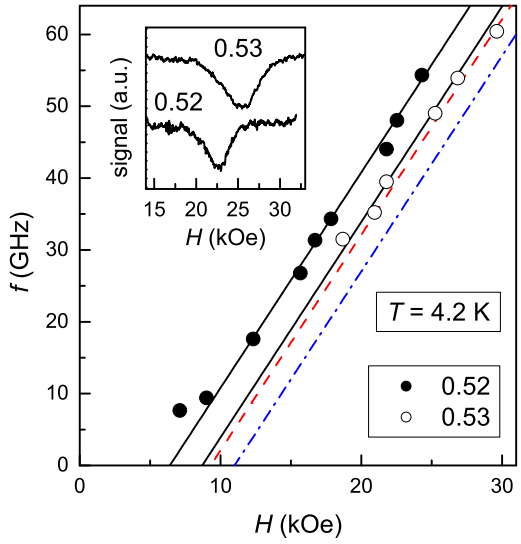

Figure 4: Dependence of the resonance frequency on the magnetic field applied normal to the film plane for samples with $x = 0.52$ and $x = 0.53$ at $T = 4.2$ K. Points are experimental data; solid lines are the theoretical curves according to Eq.(3). The dashed (red) and dash-dotted (blue) lines would correspond to the samples with $x = 0.52$ and $x = 0.53$ respectively if we considered $K_{\perp}M = K_{\|}M$ (see details in text). The inset demonstrates examples of the experimental resonance spectra at frequency 49 GHz.

ficient, $K_{\perp}M$ is the effective field of hard axis magnetic anisotropy. Due to this anisotropy, the FMR line in perpendicular geometry is shifted to the region of larger fields comparing the paramagnetic case $f = \gamma H$. This behavior is opposite to the case of the parallel geometry (Eq.(1)) where the FMR line was shifted to lower fields (Fig.1). Eq.(3) is applicable in magnetic fields exceeding the saturation field $H_S = K_{\perp}M$ while below this value $f_{\perp} = 0$.

Without the crystal structure driven magnetic anisotropy contribution, $K_{\perp} = K_{\|} = 4\pi$ and Eq.(3) transforms into the Kittel formula for the FMR frequency, when applied field H lies normally to the thin film plane [13]. If we take into account only the second order crystal structure driven magnetic anisotropy contributions to describe the total magnetic anisotropy in our system, the coefficient $K_{\perp}$ coincides with $K_{\|}$ [12].

In agreement with Eq.(3), the experimental $f_{\perp}(H)$ dependencies are linear in the region of high frequencies and fields (Fig.4). Nevertheless, the $K_{\perp}M$ parameter differs from the $K_{\|}M$ parameter. It is seen from Fig.4 that the experimental $f_{\perp}(H)$ dependencies are poorly described using for the $K_{\perp}M$ parameter the $K_{\|}M$ value obtained in the parallel geometry. For both samples, the $K_{\perp}M$ parameter is less than $K_{\|}M$ but exceeds the $4\pi M$ value obtained from static magnetization measurements (see Table 1).

Following the simplest phenomenological approach of Appendix A, the difference between $K_{\perp}$ and $K_{\|}$ can be attributed to the effect of a higher order uniaxial magnetic anisotropy of the sample. Here the term "uniaxial anisotropy" means that the magnetic energy expression has a uniaxial symmetry, i.e. it is invariant with respect to arbitrary rotations about the axis z normal to the sample plane. The anisotropy order is defined by the power of z-component of magnetization in the energy expression.

Taking into account the second order easy plane anisotropy and neglecting higher than fourth order terms of uniaxial anisotropy (see Appendix A), the relation between the $K_{\perp}M$ and $K_{\|}M$ effective fields has the form:

$$K_{\perp}M = K_{\|}M + \frac{4K_2}{M}, \qquad (4)$$

where K_2 is the fourth-order constant of crystal structure driven magnetic anisotropy. Thus, Eqs.(1–4) are similar to those used in Ref. [14] with a little different definition of the K_1 and K_2 constants.

Note that a more complex description by means of two independent fourth-order phenomenological constants is also possible by presuming a tetragonal-like character of the film distortion. However, it is beyond the scope of the current paper.

The obtained low-temperature values of the K_1 and K_2 constants are given in Table 1. The positive sign of the K_1 constant

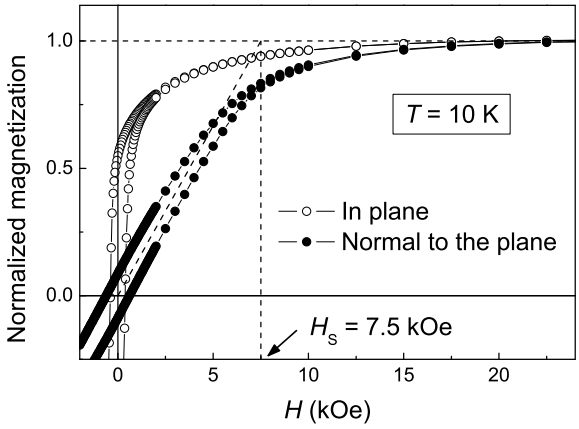

Figure 5: Hysteresis loops of the sample with $x = 0.52$ in case of the field applied in the film plane and normal to it at $T = 10$ K.

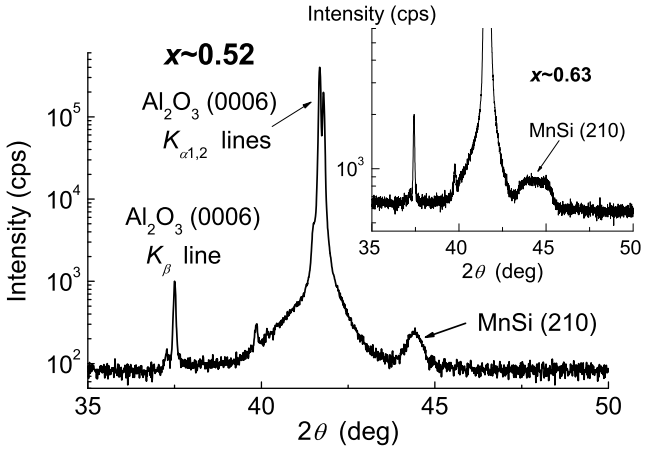

Figure 6: The X-ray diffraction pattern for the Mn_xSi_{1-x}/Al_2O_3 structure with $x \approx 0.52$. The inset shows the XRD curve for sample with $x \approx 0.63$.

corresponds to a second-order easy plane contribution into the total magnetic anisotropy of the film. The negative sign of the K_2 constant corresponds to a fourth-order easy axis contribution into the total magnetic anisotropy of the film.

As an additional demonstration of the role of magnetic anisotropy effects in our system, the low-temperature magnetization curve for the sample with $x \approx 0.52$ was measured in the field applied perpendicular to the sample plane (Fig.5). If only the second-order easy plane anisotropy takes place, the magnetization must depend on the magnetic field linearly below the saturation field $H_S = K_{\|}M$. The anisotropy of higher orders results in a nonlinearity of the magnetization curve. In this case the saturation field is defined by $H_S = K_{\perp}M$.

The experimental magnetization curve (Fig.5) shows a smooth approach to saturation. Moreover, there is noticeable hysteresis of the $M(H)$ curve (the coercive field $H_C \approx 0.65$ kOe). Linear extrapolation of the initial part of the magnetization curve leads to saturation field $H_S \approx 7.5$ kOe. The obtained value is smaller than the $K_{\|}M$ observed in FMR experiments, but larger than the $K_{\perp}M$. Thus, there is only some qualitative agreement of static magnetization and resonance data. The static magnetization curves confirm the existence of significant second-order easy plane anisotropy, but allow for neither confirmation nor rejection our assumption about the effect of the higher order contributions of crystal structure driven magnetic anisotropy on the total magnetic anisotropy of the system.

3.2. Structure investigations

The results of X-ray diffraction measurements for the $Mn_xSi_{1-x}/Al_2O_3(0001)$ structure ($x \approx 0.52$) are shown in Fig.6. The diffraction curve contains strong reflection peaks from $Al_2O_3(0006)$: $2\theta = 41.68°$ for the $CuK_{\alpha 1}$ line, $2\theta = 41.78°$ for the $CuK_{\alpha 2}$ line, and $2\theta = 37.5°$ for the line $CuK_{\beta 1}$. In addition to these peaks, this curve contains a broad peak from the ε-MnSi(210) film with B20 structure for the CuK_{α} line at $2\theta = 44.43°$.

The integral characteristic of the film's structural quality is the rocking curve width at half maximum ($FWHM_{\omega}$). For the film under study, the $FWHM_{\omega}$ parameter at $2\theta = 44.43°$ is $\Delta\omega \approx 0.4°$, whereas the $FWHM_{\omega}$ value for the single-crystalline film of the same thickness should be about 250 seconds of arc. Such a broad peak is a signature of a pronounced mosaicity and imperfection of the film structure, in particular, caused by the lattice constant mismatch between Al_2O_3 substrate and MnSi film as well as by the Mn excess (for MnSi with B20 structure, the lattice constant $a \approx 4.56$ Å; for Al_2O_3 $a \approx 4.76$ Å). At increasing Mn content the ε-MnSi(210) peak transforms to a "flat hill" about 2° wide at $x \approx 0.63$ (see inset in Fig.6).

To obtain further insight into peculiarities of the film structure, we analyze AFM and MFM images of the sample surface (see Fig.7). The AFM and MFM measurements were performed in ambient conditions for the Mn_xSi_{1-x} film with $x \approx 0.52$ and $T_C \approx 330$ K (magnetization data are shown in Fig.3). For receiving the MFM images (Fig.7b), the two-pass technique (lift-mode) was used. The height of lift on the second pass was about 30 – 50 nm. Change of the probe oscillation phase was recorded at the fixed pump frequency. The light regions on the MFM images correspond to an increase of the phase arising at a reduction of the probe resonant frequency which is caused by its attraction to the surface. Therefore, light regions on the MFM images display the areas where the probe is attracted to the sample, and dark strips show the areas where such the attraction becomes weak or is absent. Magnetic images do not depend on the sample previous history, i.e. they do not change at preliminary magnetization of the sample in this or that direction. The saturation magnetization of the sample under conditions of measurements ($T \approx 290$ K) is about 100 emu/cm^3, and its coercitivity is a fortiori less than 50 Oe (see Fig.3 and Ref. [6]). In this situation, the local reversal magnetization of the sample in the field of MFM probe is possible, leading to its attraction.

According to AFM results, the depth of weakly pronounced inter-block interfaces (thin lines in Fig.7a) does not exceed 2 nm, while strongly pronounced inter-crystallite interfaces (thick lines) have the form of cavities with the depth of

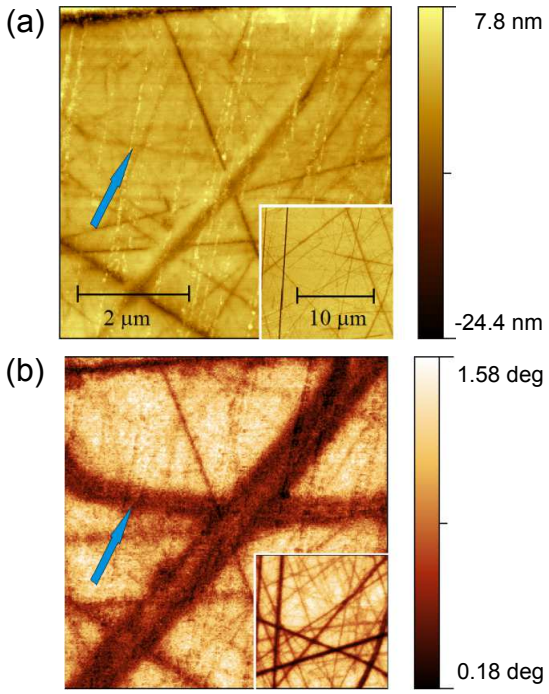

Figure 7: AFM (a) and MFM (b) images for the Mn_xSi_{1-x} film with $x \approx 0.52$ and $T_C \approx 330$ K. The light regions in the MFM image are the attracting magnetic areas. Dark regions are areas in which there is no MFM probe attraction. The arrow shows the interface between crystallites in case when it is poorly appeared in AFM mode (a) while it is obvious in MFM mode (b). Insets in Figs.7a and b demonstrate the fragments of AFM and MFM images, respectively, at large film surface scanning area $20 \times 20\ \mu m^2$.

$<$ 10 nm at the 70 nm thickness of the film. Comparison of AFM and MFM images shows that the positions of inter-crystallite interfaces correlate on the whole with dark strips in MFM images (Fig.7b). However, the width of these strips ($\sim 0.5\ \mu$m) considerably exceeds the width of lines ($\leq 0.1\ \mu$m) separating blocks (Fig.7a) in the AFM images. Moreover, there exist inter-crystallite interfaces which are almost not revealed in AFM images (shown by arrow in Fig.7a) in which, however, magnetic heterogeneity (dark strips in Fig.7b) is brightly expressed.

3.3. Possible origin of magnetic anisotropy

The itinerant cubic ferromagnet singe-crystal MnSi with B20 structure has a weak forth-order cubic magnetic anisotropy. But in case of a thin epitaxial MnSi film deposited on a thick substrate, the induced uniaxial magnetic anisotropy can be essential due to the strain caused by lattice mismatch between the film and the substrate (see [15] and references therein).

In our case, sufficiently large mismatch ($\approx$ 4 %) between the Al_2O_3 substrate and Mn_xSi_{1-x} film is realized. It is one of the main reasons for polycrystallinity of the grown film and thus initiates an existence of inter-crystallite and crystallite-substrate strain, producing crystal twin planes or inter-crystallite boundaries [16] (below we will use a unified term "plane defect").

XRD measurements clearly show that Mn_xSi_{1-x} crystallites are ordered normally to the surface of Al_2O_3 substrate, i.e. the grown films are textured (have a mosaic type). According to AFM-MFM images, the characteristic size of crystallite is about 1 μm. Obviously, in the frame of used methods we are unable to adduce direct experimental proofs of the strain inside our films; so, our supposal should be verified in future studies. However, it is well known that mechanical strain on the plane defect can induce elastic or plastic deformation (even dislocation) near this defect [16]. Following this paradigm, at least a part of thin lines (one of them is indicated in Fig.7a by arrow) may be possibly associated with the projections of plane defects with elastic strains on the film surface. Some lines (not shown in Fig.7) have a profound cavity shape and may be possibly attributed to the plane defects with strong non-elastic deformations or dislocations in the film.

The MFM data shed light on the magnetic structure of the film surface, while their interpretation seems to be ambiguous. A single-domain thin film with strong easy-plane anisotropy does not exhibit local reversal magnetization in the field of MFM probe, so the MFM foreground color should look like homogeneously dark. However, in our experiments the MFM signal is locally dark only nearby the lines possibly corresponding to projections of plane defects, as the probe approaches them, while it remains light far from them. A possible reason for such the effect is due to the significant enhancement of magnetic anisotropy near the plane defects in the film. This enhancement may be provided by an increase of anisotropic (for example, spin-orbit) component of effective exchange coupling between local magnetic moments of Mn-containing nanometer scale defects, due to strong crystal potential distortions near the plane defect in the nonstoichiometric Mn_xSi_{1-x} alloy. Following our supposition, the "local" axes of magnetic anisotropy are oriented normally to the plane defect, i.e. lie in most part in the film plane. The plane defects are randomly distributed in the film, they strongly pin local magnetic moments of Mn-containing defects and block a local reversal magnetization in MFM measurements.

The plane defect driven magnetic anisotropy mechanism does not qualitatively contradict to the above performed FMR data and their interpretation in frame of the phenomenological description of Appendix A. In Appendix B, we propose a simple quantum mechanical model of randomly distributed plane defects having spin-orbit coupling with the matrix of a weak itinerant ferromagnet. By means of this model, we support the phenomenological approach of Appendix A. In particular, the model predicts essential second order easy plane anisotropy contribution with $K_1 > 0$ and the additional forth order uniaxial anisotropy contribution with $K_2 < 0$. However, the ratio $|K_2|/K_1$ estimated from the model is $|K_2|/K_1 \sim 10^{-3} - 10^{-4}$; this is much less than the value $|K_2|/K_1 \sim 0.2 - 0.4$ found from the experiment (see Table 1). The possible reason of this disagreement is the used perturbation approach (see Appendix B) as well as the strain between crystallites and the substrate which is neglected in the proposed model. At the same time, it should be kept in mind that phenomenological description of Appendix A is developed for a purely homogeneous case, i.e. does not consider distribution of local anisotropy in the plane and on the film thickness. Therefore, the constants K_1 and K_2 found with its help have only an efficient character.

4. Conclusions

In this work, for thin films of nonstoichiometric Mn_xSi_{1-x} alloys with different manganese content ($x \approx 0.44 - 0.63$) the FMR measurements were performed in the wide range of frequencies ($f = 7 - 60$ GHz) and magnetic fields ($H = 0 - 30$ kOe). For samples with $x \approx 0.52 - 0.55$, the FMR data confirm the early reported FM order with high Curie temperatures $T_C \sim 300$ K [6, 7]. Earlier, we have explained the appearance of such FM order in Mn_xSi_{1-x} films in frame of a non-conventional defect-induced carrier-mediated mechanism [3].

Further to the fact of FM order itself, studied samples also demonstrated in FMR measurements an intricate character of magnetic anisotropy, which can be described in a phenomenological way as a combination of two contributions: the second order easy plane anisotropy component and the forth order uniaxial anisotropy component with easy direction normal to the film plane. In frame of above mentioned assumption we attribute this magnetic anisotropy to the existence of a well-pronounced mosaic (polycrystalline) structure of the films. We believe that such a mosaic structure is revealed in presented XRD and AFM measurements, be accompanied by the strain between crystallites and/or crystallites-substrate. Following our model, these local strain can initiate an enhancement of the spin-orbital anisotropic component of exchange interaction between the local moment on the point magnetic defect and itinerant electron spin in the matrix (see Appendix B). This enhancement becomes apparent as a pinning of local magnetic moments in the MFM images.

We hope that the combination of FMR, XRD, AFM and MFM methods showed its efficiency in the study of nonstoichiometric Mn_xSi_{1-x} alloys as a new class of high-temperature FM semiconductors with unusual properties.

Acknowledgments

Authors are grateful to Dr. Vasiliy Glazkov for assistance in carrying out low-temperature FMR measurements in the region of high fields. We express our gratitude to Dr. Alexei Temiryazev for AFM and MFM measurements. We would also like to thank him as well as Dr. Dmitry Kholin and Dr. Elkhan Pashaev for fruitful discussions of FMR and XRD results.

The work was partly supported by the RFBR (grant Nos. 15-07-01170, 14-07-91332, 14-07-00688, 13-07-00477, 15-29-01171, 14-47-03605, 15-07-04142), NBICS Center of the Kurchatov Institute. The work at HZDR is financially supported by DFG (ZH 225/6-1)

Appendix A. FMR in magnetic film with perpendicular anisotropy

Taking into account the perpendicular uniaxial anisotropy, the magnetic energy density of a ferromagnetic film is given by the following expression:

$$E = -\mathbf{H}\cdot\mathbf{M} + 2\pi M_z^2 + E_A(M_z), \tag{A.1}$$

where the first term is Zeeman energy in magnetic field, the second term is shape anisotropy of the sample ("demagnetization energy") and the last term represents general form of uniaxial anisotropy energy with the anisotropy axis oriented along vector $\mathbf{z}$ normal to the film plane.

Neglecting dissipation, the precession of the magnetic moment is determined by the Landau-Lifshitz equation:

$$\frac{\partial \mathbf{M}}{\partial t} = \gamma[\mathbf{M}\times\mathbf{H}_{\text{eff}}], \tag{A.2}$$

where the effective field:

$$\mathbf{H}_{\text{eff}} = -\frac{\partial E}{\partial \mathbf{M}} = \mathbf{H} - 4\pi M_z\mathbf{z} - \frac{\partial E_A}{\partial M_z}\mathbf{z}. \tag{A.3}$$

Resonance frequency is defined as eigenfrequency of the system (A.2) after its linearization near equilibrium orientation of the $\mathbf{M}$ vector. In sufficiently large fields exceeding the saturation field, the static magnetization is oriented along the magnetic field $\mathbf{M}\|\mathbf{H}$. Taking into account this condition, in case of the field applied in the film plane, the resonance frequency is defined by Eq.(1), where:

$$K_\| M = 4\pi M + M\left(\frac{\partial^2 E_A}{\partial M_z^2}\right)_{M_z=0}. \tag{A.4}$$

When the field is applied perpendicular to the film plane, the resonance frequency is defined by Eq.(3), where:

$$K_\perp M = 4\pi M + \left(\frac{\partial E_A}{\partial M_z}\right)_{M_z=M}. \tag{A.5}$$

Thus, in the presence of the uniaxial anisotropy the $K_\|$ and $K_\perp$ parameters generally speaking do not coincide. Writing the $E_A(M_z)$ function in the form of decomposition:

$$E_A = K_1\cos^2\theta + K_2\cos^4\theta + K_3\cos^6\theta + \cdots, \tag{A.6}$$

where $\cos\theta = M_z/M$, Eq.(A.4) transforms into (2) and Eq.(A.5) takes form:

$$K_\perp M = 4\pi M + \frac{2K_1}{M} + \frac{4K_2}{M} + \frac{6K_3}{M} + \cdots \tag{A.7}$$

If the sixth and higher order anisotropy constants are negligible, Eq.(A.7) and Eq.(2) lead to the expression (4).

Appendix B. Microscopic approach

Self-consistent theory of spin fluctuations in the homogeneous itinerant FM [3] is based on the simple model Hamiltonian of interacting fermions:

$$\mathcal{H}_0 = \sum_\alpha \int \Psi_\alpha^+(\mathbf{r})\varepsilon(\mathbf{k})\Psi_\alpha(\mathbf{r})d\mathbf{r} + \tag{B.1}$$
$$+ \sum_{\alpha,\beta}\int \Psi_\alpha^+(\mathbf{r})\Psi_\alpha(\mathbf{r})U(\mathbf{r}-\mathbf{r}')\Psi_\beta^+(\mathbf{r}')\Psi_\beta(\mathbf{r}')d\mathbf{r}d\mathbf{r}',$$

where $\Psi_\alpha^+(\mathbf{r})$ and $\Psi_\alpha(\mathbf{r})$ are creation and annihilation operators of fermions, $\varepsilon(\mathbf{k})$ is fermions spectrum, $\mathbf{k} = -i\partial/\partial\mathbf{r}$ is operator

of quasi momentum, $(\mathbf{r},\mathbf{r}')$ are three-dimensional space vectors, (α,β) are spin indices, $U(\mathbf{r}-\mathbf{r}')$ is effective potential of fermions interaction. Hamiltonian (B.1) is spin-rotation invariant and does not contain relativistic contributions in the fermions spectrum and effective interaction.

Let us modify Hamiltonian (B.1) for a case of mosaic film of itinerant FM deposed on the non-magnetic substrate. We suppose that this film is composed of macroscopic grains with characteristic size l in the film plane and nearest neighbored grains are separated one from other by a narrow interfacial region with characteristic thickness $d \ll l$. Notice that (d,l) significantly exceed the lattice parameter a. The grain boundaries are orthogonal to the film plane throughout all the film thickness and form an arrow of two-dimensional defects inside the film. The crystal potential in the interfacial region significantly differs from the potential inside the grains due to broken chemical bonds, inter grain clustered aggregates, mechanical strains etc. and thus strongly modifies the fermions motion. To model the effect of interfacial boundaries on the fermions behavior in itinerant FM, we treat these boundaries as non-magnetic macroscopic plane defects embedded into the homogeneous matrix and introduce additional term in the Hamiltonian of our system:

$$\mathcal{H}_1 = \sum_{\alpha,\beta,,n} \int \Psi^+_\alpha(\mathbf{r})\{[V_n I + \mathbf{D}_n\cdot\boldsymbol{\sigma}]\delta(\boldsymbol{\rho}-\boldsymbol{\rho}_n)\}_{\alpha\beta}\Psi_\beta(\mathbf{r})d\mathbf{r}. \quad \text{(B.2)}$$

Here $\delta(x)$ is delta-function, $\mathbf{r} = (\boldsymbol{\rho},\mathbf{z})$, two-dimensional vector $\boldsymbol{\rho}_n$ defines the n-th plane defect position in the film, axis $\mathbf{z}$ is orthogonal to the film plane, $\boldsymbol{\sigma}$ is vector composed from the Pauli matrices, V_n and $\mathbf{D}_n$ are respectively scalar (Coulomb) and vector (spin-orbit) components of the n-th plane defect potential. The component $\mathbf{D}_n$ may be expressed in the Bychkov-Rashba form as $\mathbf{D}_n = \eta[\mathbf{e}_n\times\mathbf{k}]$, where parameter η is proportional to the fine structure constant and gradient of interface potential, $\mathbf{e}_n$ is unit vector normal to the n-th defect plane [3].

Effect of the bulk magnetic defects with local spins $\{\mathbf{S}_j\}$ on the behavior of fermions in itinerant FM is traditionally considered within the Hamiltonian:

$$\mathcal{H}_2 = \sum_{\alpha,\beta,,j} \int \Psi^+_\alpha(\mathbf{r})\{[J_j\mathbf{S}_j\cdot\boldsymbol{\sigma}]\delta(\mathbf{r}-\mathbf{r}_j)\}_{\alpha\beta}\Psi_\beta(\mathbf{r})d\mathbf{r}. \quad \text{(B.3)}$$

Here J_j is corresponding exchange coupling integral, local spins $\{\mathbf{S}_j\}$ are randomly distributed in the three-dimensional fermions matrix with the mean inter-spin distance b, $a \ll b \ll (d,l)$.

From the total Hamiltonian of the system, $\mathcal{H} = \mathcal{H}_0 + \mathcal{H}_1 + \mathcal{H}_2$, it is possible to obtain the free energy functional $\Phi\{\mathbf{m}(\mathbf{r}),\mathbf{S}(\mathbf{r})\}$ of itinerant FM with both 2D macroscopic nonmagnetic defects and microscopic 3D magnetic defects as a series expansion in terms of the magnetic moment densities of itinerant fermions $\mathbf{m}(\mathbf{r})$ and local spins $\mathbf{S}(\mathbf{r})$. The form of $\Phi\{\mathbf{m}(\mathbf{r}),\mathbf{S}(\mathbf{r})\}$ depends on the studied temperature region and relative contributions of different terms in the Hamiltonian $\mathcal{H}$. Early in Refs. [3], we analyzed $\Phi\{\mathbf{m}(\mathbf{r}),\mathbf{S}(\mathbf{r})\}$ at the high-temperature region $T > T_C$, where T_C is the global Curie temperature of the system, completely neglecting the term $\mathcal{H}_2$, i.e. preserving spin-rotation invariance. Moreover, we revealed in Refs. [3] a drastic enhancement of exchange coupling between local spins of defects due to the effect of itinerant fermions spin fluctuations and derived corresponding expression for T_C.

In this paper, we analyzed $\Phi\{\mathbf{m}(\mathbf{r}),\mathbf{S}(\mathbf{r})\}$ below the global Curie temperature, in the temperature range $T_{SF} < T < T_C$, where T_{SF} is characteristic temperature of the freezing of itinerant fermions spin fluctuations. Without local spins, i.e. in the purely itinerant FM, T_{SF} should be the Curie temperature [3]. In the temperature region under consideration, the mean field approximation for the spin densities $\mathbf{m}(\mathbf{r}) = \mathbf{m}$ and $\mathbf{S}(\mathbf{r}) = \mathbf{M}$ seems to be reasonable on the spatial scale exceeding the characteristic lengths (b,d,l) of both micro- and macroscopic defects. Thus, taking into account all the terms in the Hamiltonian $\mathcal{H}$, after the micro- and macroscopic defect distribution averaging, we can obtain an expression for $\Phi\{\mathbf{m},\mathbf{M}\}$ as a series expansion in terms of $\mathbf{m}$ and $\mathbf{M}$. Generally speaking, this expression is cumbersome, but here we take interest only to the terms in $\Phi\{\mathbf{m},\mathbf{M}\}$ dependent on the directions of vectors $\mathbf{m}$ and $\mathbf{M}$. Let us assume that averaged local spin density $\mathbf{M}$ is saturated in the considered temperature region and does not change its absolute value M. In that case we can simplify our analysis omitting in $\Phi\{\mathbf{m},\mathbf{M}\}$ the terms independent of the $\mathbf{M}$ direction. In the fourth order in $\mathbf{m}$ and first order in $\mathbf{M}$, we can show using conventional diagram techniques for the free energy functional [3], that:

$$\begin{aligned}\Delta\Phi\{\mathbf{m},\mathbf{M}\} &= \Phi\{\mathbf{m},\mathbf{M}\} - \Phi_0\{\mathbf{M}\} = \\ &= \Phi_0\{\mathbf{m}\} + \Phi_1\{\mathbf{m}\} + \delta\Phi\{\mathbf{m},\mathbf{M}\}, \quad \text{(B.4)}\\ \Phi_0\{\mathbf{m}\} \approx A_1 m^2 + A_2 m^4,&\quad \Phi_1\{\mathbf{m}\} \approx B_1 m_z^2 + B_2 m_z^4,\\ \delta\Phi\{\mathbf{m},\mathbf{M}\} &\approx \lambda\mathbf{m}\cdot\mathbf{M}.\end{aligned}$$

The $\Phi_0\{\mathbf{M}\}$ term simply shift the free energy scale and does not takes interest for us, $\Phi_0\{\mathbf{m}\}$ and $\Phi_1\{\mathbf{m}\}$ are respectively isotropic and anisotropic in $\mathbf{m}$ contributions of itinerant fermions, $\delta\Phi\{\mathbf{m},\mathbf{M}\}$ is contribution of exchange coupling between itinerant fermions spins and magnetic defects local spins. The coefficients in formulas (B.4) can be estimated in the temperature region $T_{SF} < T < T_C$ (see Refs. [3]) as:

$$\begin{aligned}A_1 &\approx W^{-1}(\nu_F Q_{SF}/W)^2[\zeta(0)/\zeta(T)]^2,\\ A_2 &\approx W^{-3}, \qquad \lambda \approx J(a/b)^3 W^{-2},\end{aligned} \quad \text{(B.5)}$$

$$\begin{aligned}B_1 &\approx W^{-1}(d/l)(\eta/\nu_F)^2,\\ B_2 &\approx -W^{-3}(d/l)(\eta/\nu_F)^4.\end{aligned} \quad \text{(B.6)}$$

Here W is energy scale of the order of fermions bandwidth, ν_F is the Fermi velocity, Q_{SF} is the cut-off wave vector of itinerant fermions spin fluctuations, $\zeta(0) \approx \nu_F/W$, $\zeta(T)$ is correlation length of itinerant fermions spin fluctuations, renormalized by a scattering on the Coulomb component of macroscopic defects potential V. This scattering is not explicitly included in formulas (B.5), since at considered temperatures and relations between the parameters of our model $(d/l) \ll 1$, $[d/\zeta(0)] \ll 1$, $(V/W)^2 \ll 1$ it does not lead to new physical effects.

It is seen from Eq.(B.5) and Eq.(B.6) that coefficients A_1, A_2, B_1, λ are positive in the considered temperature region, while coefficient B_2 is negative. Formally this fact is due to an interplay between different diagrams of the eighth order in

$\Phi\{\mathbf{m},\mathbf{M}\}$ series expansion in the effective perturbation field $[\mathbf{m}(\mathbf{r}) + \sum_n \mathbf{D}_n(\boldsymbol{\rho} - \boldsymbol{\rho}_n)]$, leading to appearance of the fourth order in $\mathbf{m}$ anisotropic contributions to $\Phi_1\{\mathbf{m}\}$ after averaging over macroscopic defects distribution. We do not attribute a profound physical meaning to this result, while it seems noteworthy.

Varying $\Delta\Phi\{\mathbf{m},\mathbf{M}\}$ over $\mathbf{m}$, after neglecting for simplicity the $\Phi_1\{\mathbf{m}\}$ contribution, we get in the mean field approximation for an equilibrium value $\mathbf{m}_0 \approx -\lambda/2A_1\mathbf{M}[1 - (\lambda A_2/A_1)^2 M^2]$. Substituting $\mathbf{m} = \mathbf{m}_0$ in $\Delta\Phi\{\mathbf{m},\mathbf{M}\}$ and separating isotropic and anisotropic terms, we obtain for the magnetic anisotropy energy E_A the expression (A.6) with $\cos\theta = M_z/M$ and

$$K_1 \sim B_1 m_0^2 > 0, \qquad K_2 \sim B_2 m_0^4 < 0. \tag{B.7}$$

Estimations of relative and a fortiori absolute values of K_1 and K_2 are uninformative in our model due to their very rough approximate character. Obviously, in our approach contribution of the forth order terms proportional to K_2 must be small compared with contribution of the second order terms proportional to K_1 in Eqs.(B.7) due to the used perturbation theory in the fine structure parameter:

$$|K_2|/K_1 \sim (\eta/v_F)^2 W^{-2} m_0^2 \sim 10^{-3} \div 10^{-4} \ll 1. \tag{B.8}$$

From the phenomenological model of Appendix A, to satisfy obtained FMR results we have to put $|K_2|/K_1 \sim 10^{-1}$. Thus, correspondence between Eq.(B.8) and experimental results is not yet good. This disagreement is not surprising since the developed model is based on the perturbation approach to the spin-orbit component of coupling between itinerant electron spin of the matrix and the plane defect moment, i.e. the calculated coefficients K_1 and K_2 are obtained as the lowest terms in the corresponding series expansion of the coupling energy on the spin-orbit components. For real alloys the used perturbation approach may be incorrect, but unfortunately, in the theory of itinerant ferromagnetism there exist no adequate description to take strong spin-orbit coupling into account.

References

[1] S. Zhou and H. Schmidt, Materials 3 (2010) 5054.
[2] S. Zhou, K. Potzger, G. Zhang, A. Mücklich, F. Eichhorn, N. Schell, R. Grötzschel, B. Schmidt, W. Skorupa, M. Helm, J. Fassbender, D. Geiger, Phys. Rev. B 75 (2007) 085203.
[3] V.N. Men'shov, V.V. Tugushev, S. Caprara, Phys. Rev. B 83 (2011) 035201; V. N. Men'shov and V.V. Tugushev, J. Exp. Theor. Phys. 113 (2011) 121.
[4] S. Kahwaji, R.A. Gordon, E.D. Crozier, S. Roorda, M.D. Robertson, J. Zhu, T.L. Monchesky, Phys. Rev. B 88 (2013) 174419.
[5] E.S. Demidov, V.V. Podol'skii, V.P. Lesnikov, E.D. Pavlova, A.I. Bobrov, V.V. Karzanov, N.V. Malekhonova, A.A. Tronov, JETP Lett. 100 (2015) 719.
[6] V.V. Rylkov, S.N. Nikolaev, K.Yu. Chernoglazov, B.A. Aronzon, K.I. Maslakov, V.V. Tugushev, E.T. Kulatov, I.A. Likhachev, E.M. Pashaev, A.S. Semisalova, N.S. Perov, A.B. Granovskii, E.A. Gan'shina, O.A. Novodvorskii, O.D. Khramova, E.V. Khaidukov, V.Ya. Panchenko, JETP Letters 96 (2012) 255.
[7] V.V. Rylkov, E.A. Gan'shina, O.A. Novodvorskii, S.N. Nikolaev, A.I. Novikov, E.T. Kulatov, V.V. Tugushev, A.B. Granovskii, V.Ya. Panchenko. Europhys. Lett. 103 (2013) 57014.
[8] A. Yang, K. Zhang, S. Yan, S. Kang, Y. Qin, J. Pei, L. He, H. Li, Y. Dai, S. Xiao, Y. Tian, J. Alloy. Compd. 623 (2015) 438.
[9] S.M. Stishov and A.E. Petrova, Phys. Usp. 54 (2011) 1117.
[10] J.A. Hagmann, K. Traudt, Y.Y. Zhou, X. Liu, M. Dobrowolska, J.K. Furdyna, J. Magn. Magn. Mater. 360 (2014) 137.
[11] S.V. Demishev, V.V. Glushkov, I.I. Lobanova, M.A. Anisimov, V.Yu. Ivanov, T.V. Ishchenko, M.S. Karasev, N.A. Samarin, N.E. Sluchanko, V.M. Zimin, A.V. Semeno, Phys. Rev. B 85 (2012) 045131.
[12] S.V. Vonsovskii, *Ferromagnetic Resonance* (Pergamon Press, Oxford, 1966).
[13] C. Kittel, J. Phys. Radium. 12 (1951) 291.
[14] J.-M.L. Beaujour, W. Chen, K. Krycka, C.-C. Kao, J.Z. Sun, A.D. Kent, Eur. Phys. J. B 59 (2007) 475.
[15] M.N. Wilson, A.B. Butenko, A.N. Bogdanov, and T.L. Monchesky, Phys. Rev. B 89 (2014) 094411.
[16] A.M. Kosevich, V.S. Boiko, Sov. Phys. Usp. 14 (1971) 286.